Electrodes-oxide-semiconductor device for biosensing: renewed conformal analysis and multilayer algorithm

Supplementary Material

Rémi Pampin, Jean-Pierre Raskin, Isabelle Huynen and Denis Flandre

ICTEAM Institute, ELEN Division, Place du Levant 3, B-1348 Louvain-la-Neuve, Belgium

1. Elliptic integrals asymptotic ratio

Elliptic integrals ratio evaluation usually benefits from following approximation and equivalence [1] – to within ∓ 0.5 % for $0.62 \leq k < 1$ or $0 < k' \leq 0.22$:

$$\frac{\mathrm{K}(k)}{\mathrm{K}(k')} \simeq \ln\left[4(1+k)/(1-k)\right]/\pi$$
$$\ln\left[(1+k)/(1-k)\right] \equiv 2\,\mathrm{argth}(k)$$

where $k' = \sqrt{1-k^2}$.

This applies as well to $\mathrm{K}(k')/\mathrm{K}(k)$ by simply taking the inverse of the logarithm or changing k for k' variable. Expressing elliptic *moduli* in terms of exponential or hyperbolic tangent then helps formula further reduction.

2. Conformal Mappings

2.1. Base model

Physical domain first scaling $\boldsymbol{r} = \boldsymbol{p} \cdot \mathrm{K}(\kappa)/(\frac{1}{2}\Lambda_D)$ that allows for conformal mapping must preserve $\boldsymbol{p}$-shape [2] in accordance with half-period ratio

$$\tau = \iota\ \mathrm{K}(\kappa')/\mathrm{K}(\kappa) = \iota\, H/(\tfrac{1}{2}\Lambda_D).$$

Elliptic integrals theory then relates κ modulus therein to ϑ_2 and ϑ_3 Jacobi *theta* functions through nome $q = \exp(\pi\iota\,\tau)$ as finally expressed in (B.2). With regards to implementation efficiency, $\mathrm{K}(\kappa) \equiv \frac{1}{2}\pi\,\vartheta_3^2(q)$ identity permits to advantageously rewrite $\{\boldsymbol{p} \leftrightarrow \boldsymbol{r}\}$ normalization (B.1) as a function of ϑ_3, used again in (B.2).

By principle, Schwarz-Christoffel transformations (B.2) and Article's Eq. 2 respectively articulate around poles $t_3 = 1$, $t_4 = 1/\kappa$ and ${}_{\theta,x}w_3 \equiv 1/{}_{\theta,x}k$, $w_4 \equiv 1/{}_y k$, which considering (B.3) justify *moduli* expressions in the Article.

2.2. Thin film approximation

In a thinning domain, approximating ϑ_3 identity from Table 1 as $\vartheta_3(q) \cong \sqrt{\frac{1}{2}\Lambda_D/H}$ leads to $\boldsymbol{r} \simeq \frac{1}{2}\pi\boldsymbol{p}/H$, feeding the Article's forward Equations 2. The limit of above $\tau(\kappa)$

	$k \to 0$	$k \to 1$	
$\mathrm{sn}(z,k)$	$\sin(z)$	$\tanh(z)$	
$\mathrm{sn}\left[\frac{1}{2}\mathrm{K}(k),k\right]$	$\equiv 1/\sqrt{1+k'}$		(1)
$\mathrm{sn}\left[a \pm \iota\,\mathrm{K}(k'),k\right]$	$\equiv 1/\left[k \cdot \mathrm{sn}(a,k)\right]$		(2)
$\mathrm{sn}\left[\mathrm{K}(k) \pm \iota\, b,k\right]$	$\equiv 1/\,\mathrm{dn}(b,k')$		
$\mathrm{dn}(z,k)$	1	$\mathrm{sech}(z)$	
$\vartheta_3\left(e^{-\pi/z}\right)$	$\equiv \sqrt{1/z}\ \ \vartheta_3\left(e^{-\pi z}\right)$		

	$z \leq \frac{1}{4}$	$\frac{3}{4} < z$
$\cosh\left(\frac{\pi}{2}z\right)$	$\simeq 1\ (+\frac{\pi^2}{8}z^2)$	$\to \dfrac{e^{\frac{1}{2}\pi z}}{2}$
$\sinh\left(\frac{\pi}{2}z\right)$	$\simeq \frac{\pi}{2}z$	
$1-\tanh^2\left(\frac{\pi}{2}z\right)$	$\equiv 1/\cosh\left(\frac{\pi}{2}z\right)$	

Table 1: Useful functions identities and approximations at $\pm 10\%$. Symbol ι stands for the complex imaginary unit. Also note: $\mathrm{dn}(\dots)^2 + k^2\,\mathrm{sn}^2(\dots) = 1$.

for $\kappa \to 1$ using Supplementary Section 1 further allows to extract unitary ${}^0\kappa$ asymptote:

$$\begin{aligned}\frac{1+{}^0\kappa}{1-{}^0\kappa} &\cong \frac{1}{4}\exp\left(\tfrac{1}{2}\pi\Lambda_D/H\right),\\ {}^0\kappa &\cong \tanh\left[\frac{\pi}{2H}\tfrac{1}{2}\Lambda_D - \ln(2)\right]\\ &\cong \tanh\left\{\eta\big(\Lambda_c + [\underbrace{\Lambda_g - \ln(2)/\eta}_{\Lambda_g^e}]\big)\right\}\end{aligned}$$

where $\eta = \pi/(4H)$.
Introducing t_2 and t_4 subsequent poles in the Article's Eq. 2 leads to *moduli* asymptotes after a few more trigonometric developments in transverse, as:

$$\begin{aligned}{}^0_x k &\cong \tanh(\eta\Lambda_c)\sqrt{\frac{1-\tanh^2[\eta(\Lambda_c+\Lambda_g^e)]}{1-\left\{\tanh^2[\eta(\Lambda_c+\Lambda_g^e)]\tanh(\eta\Lambda_c)\right\}^2}}\\ &\cong \frac{\tanh(\eta\Lambda_c)}{\sqrt{1+[\tanh(\eta\Lambda_c)\cosh(\eta\Lambda_g^e)+\sinh(\eta\Lambda_g^e)]^2}}\\ &\simeq \exp\left(-\eta\Lambda_g^e\right)\end{aligned}$$

altogether issuing, for $H \to 0$:

$$\begin{aligned}&{}^0_x k \simeq \exp\left[-\frac{\pi}{2H}\tfrac{1}{2}\Lambda_g + \ln(2)\right] && \to 0\\ &{}^0_\theta k = \tanh\left(\frac{\pi}{2H}\tfrac{1}{2}\Lambda_c\right) \quad \text{and} \quad {}^0_y k = {}^0\kappa\cdot{}^0_\theta k && \to 1\end{aligned}$$

Before simplifying related ${}^0CSR$ by logarithmic approximations (Supplementary Section 1), radial *modulus* is also rewritten through intermediate steps, as follows:

$${}^0_y k \cong \tanh(\eta\Lambda_c)\tanh\left\{\eta\big(\Lambda_c + [\Lambda_g - \ln(2)/\eta]\big)\right\}$$

such that

$$\begin{aligned}\frac{1+{}^0_y k}{1-{}^0_y k} &\equiv 2\cosh^2(\eta\Lambda_c)[1+\tanh(\eta\Lambda_c)\tanh(\eta\Lambda_g^e)] - 1\\ &\cong \tfrac{1}{2}\exp(2\eta\Lambda_c)[1+\tanh(\eta\Lambda_g^e)]\end{aligned}$$

and finally

$$\begin{aligned}{}^0_y CSR &\cong \frac{\frac{1}{2}\Lambda_c}{H}\\ &\quad + \frac{1}{\pi}\left\{\ln(2) + \ln\left[1+\tanh\left(\frac{\pi}{4}\frac{\Lambda_g^e}{H}\right)\right]\right\}.\end{aligned}$$

Relative ${}^0_y CSR$ formula complexity extends computability range of transverse ${}_x CSR^+ \equiv {}_\theta CSR^+ - {}_y CSR$ (eq. 1 invariant) when self and mutual couplings both tend to the parallel-plates limit:

$$\begin{aligned}{}^0_x CSR^+ &\cong \frac{1}{\pi}\left\{\ln(2) - \ln\left[1+\tanh\left(\frac{\pi}{4}\frac{\Lambda_g^e}{H}\right)\right]\right\}\\ &\to \frac{1}{\pi}\ln\left(1+e^{-\pi\frac{1}{2}\Lambda_g^e/H}\right) \approx \frac{4}{\pi}\exp(-\pi\tfrac{1}{2}\Lambda_g/H)\end{aligned}$$

– note the last change to Λ_g on lower-right corner.

In complement to ${}^0CSR$ thin-film results (Article Section 3.1.2), above *moduli* associate with asymptotes applicability thresholds. Since ${}^0_x k'|_{\Lambda_g\to\Lambda_D} \geq {}^0\kappa \geq {}^0_\theta k \geq {}^0_y k$ at worst case for $\Lambda_g \to \Lambda_D$, computation difficulty may primarily arise out of transverse *modulus*; this triggers for $\left({}^0_x k \leq \sqrt{2\xi}\right) \Leftrightarrow \left[\frac{H}{\Lambda_D} \leq \frac{-\pi}{2\ln(\xi/2)}\right]$. Solving $\left({}^0\kappa \geq 1-\xi\right)$ ends up with the same definition. It corresponds to the computability barrier for thin film CSR; however, some additionnal margin arose necessary to improve computing *precision* close to that barrier. A couple of LSB (Least Significant Bit) are typically used to keep room for computation, preventing numerical overflow. This meant here multiplying ξ by 2 or 4 in above formula – a factor four being finally included in the Article.

2.3. Infinite medium approximation

At first-order, ${}^\infty\vartheta_2 \approx 2q^{1/4}$ and ${}^\infty\vartheta_3 \approx 1$ developments together with $\mathrm{sn}(z,0) \equiv \sin(z)$ identity yield, asymptotically:

$$\begin{aligned}&{}^\infty\kappa \cong 4\exp\left(-\pi H/\Lambda_D\right) && \to 0\\ &{}^\infty_\theta k \cong {}^\infty_x k && \cong \sin\left(\frac{\pi}{2}\frac{\Lambda_c}{\Lambda_D}\right)\\ &{}^\infty_y k = {}^\infty\kappa\cdot{}^\infty_\theta k && \to 0\end{aligned}$$

Since odd *modulus* ultimately collapses to transverse component only, no further thickness-related approximation applies.

Regarding computability threshold towards zero ${}^\infty_y k \leq {}^\infty\kappa \leq {}^\infty_{\theta,x} k$, securely choosing ${}^{bnd}_y k = 4e^{-\pi/\Lambda_D}(\Lambda_c/\Lambda_D)$ upper bound permits to derive Appendix B.1 criterion as: $\left({}^\infty_y k \leq \sqrt{2\xi}\right) \Leftrightarrow \frac{H}{\Lambda_D} > \frac{1}{\pi}\left[\ln\left(4\Lambda_c/\Lambda_D\right) - \frac{1}{2}\ln(2\xi)\right]$.
Then considering first-order development $(\pi H+\Lambda_g)/\Lambda_D > -\frac{1}{2}\ln(8\xi)$ allows neglecting above right-hand side geometrical parameters ratio logarithm while finalizing the Article Section 3.1.3 worst-case condition: $\frac{H}{\Lambda_D} > -\frac{1}{2\pi}\ln(8\xi)$.

2.4. Isotropical coordinates

In order to locate *iso*-thickness ${}_\theta H_\#$ for which ground corner $p_4 = \frac{1}{2}\Lambda_D - \iota\,{}_\theta H_\#$ maps onto lower mid-segment ${}_\theta s_3 - {}_\theta s_0$, squared w_4 pole should verify, re-expressing t_4 under thin-film assumption (Article Equation 2):

$$\begin{aligned}{}^0t_4^2 &\cong 1 + 1/\sinh^2(\tfrac{\pi}{4}\Lambda_D/H) && \text{in forward mapping}\\ {}^0t_\#^2 &= ({}^0_\theta\boldsymbol{w}\,{}^0_\theta k)^2 && \text{backwards.}\end{aligned}$$

The latter can be developed after the Article's Equation B.4 backwards, using Table 1 identities (1) and (2) while noting ${}_\theta k' = \sqrt{1-{}_\theta k^2} = \mathrm{cn}(r_2, \kappa\to 1)$, such as:

$${}_\theta\boldsymbol{w}_\# = \frac{1}{{}_\theta k}\sqrt{1+\mathrm{cn}(r_2,\kappa)} \quad \text{so } {}_\theta\boldsymbol{t}_\# = \sqrt{1+\mathrm{cn}(r_2,\kappa)}$$

$$\text{where } {}^0r_2 \cong \frac{\pi}{4}\frac{\Lambda_c}{{}_\theta H_\#}, \qquad \text{then } {}^0_\theta\boldsymbol{t}_\# \cong \sqrt{1+\mathrm{sech}\left(\frac{\frac{\pi}{4}\Lambda_c}{{}_\theta H_\#}\right)}.$$

Finally, equating $t_4 = t_\#$ squared images and fixing $H = {}_\theta H_\#$ provide, after 2nd-order development: $\left({}^0t_4^2 = {}^0t_\#^2\right) \Leftrightarrow \sinh^2(\frac{1}{4}\pi\Lambda_D/{}_\theta H_\#) = \cosh(\frac{1}{4}\pi\Lambda_c/{}_\theta H_\#)$, verified at 2^{nd}-order by

$$\boxed{{}_\theta H_\# \propto \frac{\pi}{4\sqrt{2}}\Lambda_D\sqrt{\Lambda_g/\Lambda_D}.}$$

Toward infinite medium otherwise, specific *iso*depth identifies with the following:

$$\begin{aligned} ({}^\infty_{\theta,x}t)_\# &\cong \sin\left[\pi(\tfrac{1}{2} + \iota\,{}^\infty_{\theta,x}H_\#/\Lambda_D)\right] && \text{forward,} \\ {}^\infty_{\theta,x}t_\# &\cong \sqrt{1+\cos(\tfrac{1}{2}\pi\Lambda_c/\Lambda_D)} && \text{backwards,} \end{aligned}$$

verified after sinus development by ${}^\infty_{\theta,x}H_\# \cong \text{argch}({}^\infty_{\theta,x}t_\#)\times \frac{\Lambda_D}{\pi}$. Eventually, ${}^\infty_{\theta,x}t_\#$ trigonometric rewriting and 1^{st}-order development return

$$\boxed{{}^\infty_{\theta,x}H_\# \approx \frac{1}{\sqrt{2\pi}}\Lambda_D\sqrt{\Lambda_g/\Lambda_D}.}$$

This formula has been verified down to 5% gap/periodicity ratio for at worst 40% maximal error.

Associated *isotropical* abscissa ${}^\infty p_\#$ delimits near and far field fluxes on each electrode finger in infinite medium. The expression is derived similarly to above, as:

$${}^\infty p_\# = \frac{\Lambda_D}{\pi}\arcsin\left[\frac{\cos(\frac{1}{2}\pi\Lambda_g/\Lambda_D)}{\sqrt{1+\sin(\frac{1}{2}\pi\Lambda_g/\Lambda_D)}}\right]. \qquad (3)$$

First-order development of arcsinus and square root inverse give:

$$\begin{aligned} {}^\infty p_\# &\simeq \frac{\Lambda_D}{\pi}\cos(\tfrac{1}{2}\pi\Lambda_g/\Lambda_D)\left[1-\tfrac{1}{2}\sin(\tfrac{1}{2}\pi\Lambda_g/\Lambda_D)\right] \\ &\cong \frac{\Lambda_D}{\pi}\left[\cos(\tfrac{1}{2}\pi\Lambda_g/\Lambda_D) - \tfrac{1}{4}\sin(\pi\Lambda_g/\Lambda_D)\right] \\ &\cong \frac{\Lambda_D}{\pi}\left[\sin(\tfrac{1}{2}\pi\Lambda_c/\Lambda_D) - \tfrac{1}{4}\sin(\pi\Lambda_c/\Lambda_D)\right]. \end{aligned}$$

Average error then comprised between -17% and -31% for 1% to 99% metallisation ratio suggests an empirical correction factor about 1.31 to rescale around ±10%. As an alternative, Equation 3 third-order polynomial fitting performs better, though above 10% metallisation ratio, with

$${}^\infty p_\# \approx \left[-0.16\left(\frac{\Lambda_c}{\Lambda_D}\right)^2 + 0.74\frac{\Lambda_c}{\Lambda_D} - 0.01\right]\Lambda_D.$$

This abscissa is close to the central part of an electrode finger coupled to far fields. Complementarily, the width of a finger's edge coupled to near fields is then ${}^\infty_{\theta,x}\Lambda_{c\#} = \frac{1}{2}\Lambda_c - {}^\infty p_\#$, reported in the Article.

3. Partial images: discussion

Canonical Partial Capacitances are depicted in Figure 1. For non-canonical coplanar-strip devices in odd, differential mode, P.C. are disputable. For example, usual SPC tends to be casually applied to transverse ${}_xC$ while being poorly legitimate there, considering fluxes sectoral spread. Alternatively, Gevorgian et al. [4] proposed to approximate SPC-type interfaces as holding "projected stripe" (for single-gap, two fingers waveguide), disregarding fields fringing at interfaces and thereby distancing itself from genuine images methods. Although properly combining partial components from the outside-in iteratively, eliminating partial permittivities and distinguishing transverse from radial components, such formalism fails for not thin super-strata and does not provide a true solution to permittivities non-monotonic profiles.

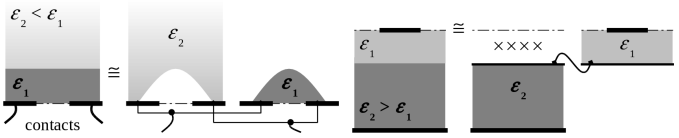

(a) Parallel-P.C. (b) Series-P.C.

Figure 1: Partial Capacitances (P.C.) principle [3].

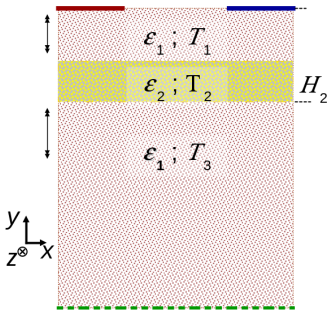

Figure 2: Multilayer test case, sliding layer 2 along {1–3} frame; $T_2 = 0.2\,\Lambda_D$, $H = \sum_n T_n = 6\,\Lambda_D$.

4. Numerical Verifications

The finer the grid, the lower the error and its slope. Conformal analysis outcomes were used to gather mesh resolution first guesses to guaranty F.E. reliability, with an initial target of 5 % flux per vertice. A median or square-root average of at least 40 to 60 elements per Λ_D was retained as fine-meshing parameter in isotropical region,

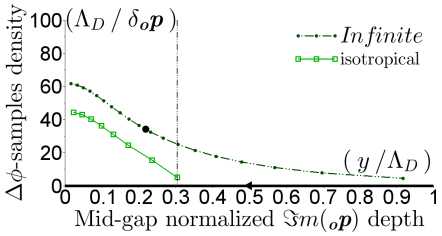

Figure 3: Mesh densities for 5% transverse flux sampling ($\Lambda_g/\Lambda_D = 0.3$) [3]. *Iso*-ordinates ${}^\infty_{\theta,x}H_\#$ (•) and ${}_\theta H_\#$ (¦) distinguish near from far fields.

Geometry	Coordinates		Resolution	
Zone	$\pm x_{max}$	$\pm y_{max}$	Δx_{max}	Δy_{max}
Coplanar	$\frac{1}{2}\Lambda_D$	${}_0H_\#$	$\Lambda_c/64$	$\Lambda_D/32$
'Sensitive'	$\frac{1}{2}\Lambda_D + 1.5{}_0H_\#$	$3\Lambda_D$	$\Lambda_c/32$	$\Lambda_D/16$
bulk	$3.5H$	H	H	$H/8$

Table 2: Mesh refinement boxes early definitions.

	Coordinates		Resolution	
Zone	$\pm x$	$(0\,;)\ y_{max}$	Δx_{max}	Δy_{max}
bulk	$\frac{1}{2}\Lambda_D$	H	$\Lambda_D/8$	$H/8$
layer$_n$	$\frac{1}{2}\Lambda_D$	$H_n\,;H_{n+1}$	$\Lambda_D/16$	$H/8$
'sense'	$\frac{1}{2}\Lambda_D$	Λ_D	$\Lambda_D/16$	$\Lambda_D/16$
fingers	$\frac{1}{2}[\Lambda_g\,;\Lambda_D]$	${}_0H_\#$	${}^\infty p_\#/32$	${}_0H_\#/16$
gap	$\frac{1}{2}\Lambda_g$	${}_0H_\#$	$\Lambda_g/256$	${}_0H_\#/32$
edges	$\frac{1}{2}\Lambda_g \pm {}^\infty_{0,x}\Lambda_{c\#}$	${}_0H_\#$	${}^\infty_{0,x}\Lambda_{c\#}/32$	${}_0H_\#/32$

Table 3: Mesh refinements final definitions.

10 to 20 mean resolution in broader 90 %-sensitive area, and below 10 toward far field (Table 2). However, verifications subsequently done by sweeping the mesh density using TCAD software indicated much higher final resolutions, summarized in Table 3.

4.1. Blume's model

Prior art model by Blume *et al.* [5] has been assessed for monolayers in Figure 4 and multilayers in Figure 5. Errors were truncated at 100% for better display. In addition to not explicitly computing the radial component, modeling of conductor-backed substrates is not convincing (Fig. 4-a and -b). On the contrary, bare backside models perform very as well as ours – unless early forcing thin-film approximation at small gap (-c′). So-called "effective" permittivity computation may be considered positively for

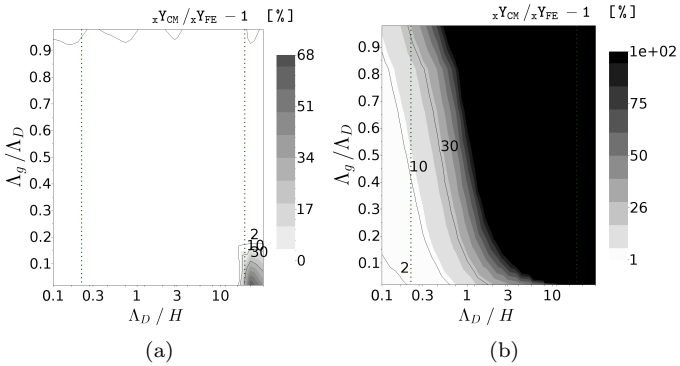

Figure 4: Monolayer Blume's model transverse errors relative to F.E. verification benches, without (a) or with (b) backside contact. Radial coupling not computed. Shades of gray and isocontours indicate the errors [%]. Figures made of 14 × 7 tests (abscissa × ordinates); $\Lambda_D = 1$ µm, $\varepsilon = 1$.

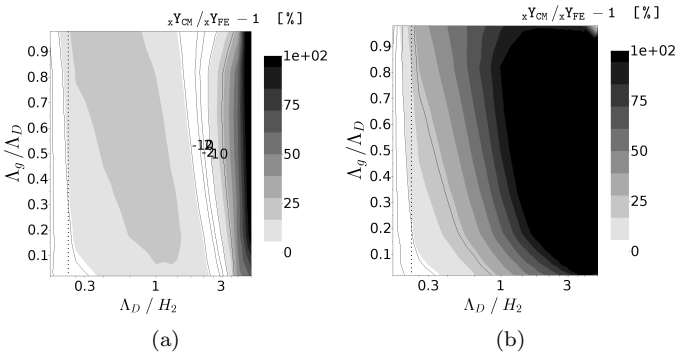

Figure 5: Three-layers transverse errors *vs.* F.E. according to Blume partial permittivities algorithm – using our monolayer model still. Dielectric stacks are (a) $\varepsilon = \{3 \setminus 1 \setminus 3\}$ on open backside, or (b) $\varepsilon = \{1 \setminus 3 \setminus 1\}$ closed on back contact. 14 abscissa × 7 ordinates.

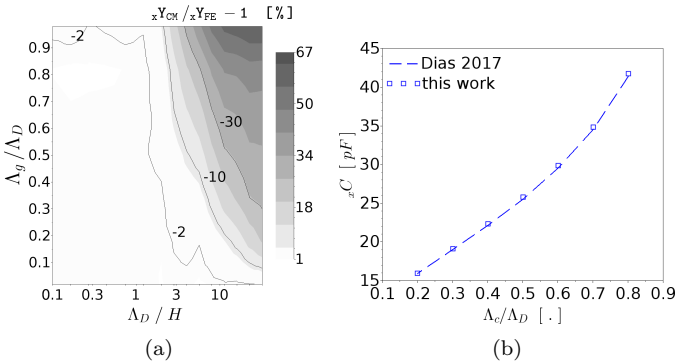

Figure 6: Open backside transverse-only capacitance at one side of an IDA, with Dias & Igreja [6] recursive images. (a) Errors relative to F.E. for a monolayer $\{T_1 = H;\ \varepsilon_1 = 1\}$, emulated here by a bilayer with ideally-insulating secondary medium $\{T_2 = 10\,\Lambda_D;\ \varepsilon_2 = 0\}$ – mimicking Neumann condition at depth T_1. (b) Experimental device capacitance with $\{T_1 = 5\,\Lambda_D;\ \varepsilon_1 = 5.4\}$ first layer, $\{T_2 = 10\,\Lambda_D;\ \varepsilon_2 = 1\}$ second, and 1.08 extrusion length.

multilayer combination on open backside, but not with back contacting (Fig. 5-a and -b, resp.).

4.2. Dias' model

Although they could be classified as numerical methods rather than close-form approaches, recursive images were tried-out for completeness [6]. Since they rely on meshing, the vertical axis sampling interval for transverse capacitance evaluation was calculated as:

$$\mathrm{d}y = min[\Lambda_c; \Lambda_g; min(H_n)]/100.$$

The number of iterations (or recursions) is in the order of a dozen.

4.2.1. Monolayer

Figure 6-a reports a similar test case as our own Article's Figure 6-c (Section 5.1.1), but with recursive images. Their difficulties at thin layer and fingers could come from either the mesh, or from emulating an ideally-open monolayer by a fictitious bilayer with zero second permittivity. Although the latter is purely theoretical, it is an insightful

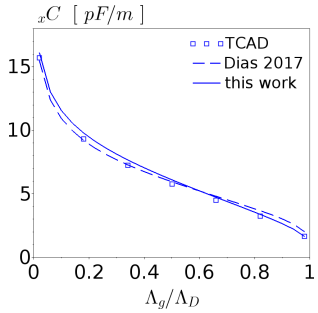

Figure 7: Transverse capacitance with Dias *et al.* [6] bilayer: $\{T_1 = 0.2\,\Lambda_D\ ;\ \varepsilon_1 = 3\}$ first stratus, $\{T_2 = \infty\ ;\ \varepsilon_2 = 1\}$ second.

sanity check to challenge models logic and limits – here checking ideal Neumann boundary condition at support's backside. Figure 6-b is taken from Dias & Igreja experimental bilayer test case on borosilicate glass followed by infinite air, that is: $\Lambda_D = 400\,\mu$m, thicknesses $\{2\,\text{mm} \setminus \infty\}$, relative permittivities $\{5.4 \setminus 1\}$, and an extrusion length of 54 fingers $\times$ 2 cm array length. Recursive images results are in good agreement, confirming their correct implementation – at least for two layers. The number of computation points is however ten to a hundred thousand higher for recursive images than for our model, due to meshing.

4.2.2. Bilayer

A bilayer having $T_1 = 0.2\,\Lambda_D$ and $\varepsilon_1 = 3$, under infinite top air, was evaluated. Results match our model well (Figure 7), but with ten thousand times more computation points. The arbitrary need for a large-permittivity substrate in that approach is further questionable, moreover as it may be tuned. This enforces Dirichlet condition on the IDA plane between fingers instead of usual Neumann insulation.

Since mesh setup, model's assumptions (see the Article Section 5.1.2) and maturity – according to its own authors – seemed questionable, our evaluations were stopped here.

References

[1] S. I. Abramowitz M., Handbook Of Mathematical Functions with formulas, graphs, and mathematical tables, Vol. 55 of Applied Mathematics, Dover Publ. Inc., N. Y., 1972 / 1992.

[2] R. Igreja, C. Dias, Analytical evaluation of the interdigital electrodes capacitance for a multi-layered structure, Sens. Actuators, A 112 (2) (2004) 291 – 301. doi:10.1016/j.sna.2004.01.040.

[3] R. S. Pampin, Biocapteurs à réseaux d'électrodes isolées sur semiconducteur actif, Ph.D. thesis, UCL - SST/ICTM/ELEN - Pôle en ingénierie électrique (2012).
URL http://hdl.handle.net/2078.1/114724

[4] S. Gevorgian, et al., Basic parameters of coplanar-strip waveguides on multilayer dielectric/semiconductor substrates. part 2: Low permittivity superstrates, IEEE Microw. Mag. 4 (3) (2003) 59–78. doi:10.1109/MMW.2003.1237478.

[5] S. O. Blume, et al., Modelling the capacitance of multi-layer conductor-facing interdigitated electrode structures, Sens. Actuators, B 213 (2015) 423 – 433. doi:10.1016/j.snb.2015.02.088.

[6] C. Dias, R. Igreja, A method of recursive images to obtain the potential, the electric field and capacitance in multi-layer interdigitated electrode (IDE) sensors, Sens. Actuators, A 256 (2017) 95 – 106. doi:10.1016/j.sna.2017.01.021.